**GSA DATA REPOSITORY 2017035**

Supplementary material for **"Foreland exhumation controlled by crustal thickening in the Western Alps"**

## Section DR1: Sample locations and characteristics

**Figure DR1:** Stratigraphic log of Faucon du Caire and Esclangon Tertiary basins overthrust by the Digne nappe.

**Table DR1:** Sample descriptions and locations

## Section DR2: Analytical methods and thermal modeling

**Mineral separation**

**Apatite (U-Th-Sm)/He methods**

**Table DR2:** Apatite (U-Th-Sm)/He data

**Figure DR2:** AHe age as a function of the effective uranium (eU) content, for the (A) Faucon du Caire and (B) Esclangon sites.

**AFT dating methods**

**Table DR3:** Apatite fission-track data.

**Figure DR3:** Radial plot representation of the AFT counting data of Esclangon and Faucon du Caire samples.

**Thermal history modeling**

## Section DR3: Estimates of the emplacement time and thickness of the Digne thrust-sheet

**Digne thrust-sheet emplacement time**

**Digne thrust-sheet thickness estimation**

**Section DR1: Sample locations and characteristics**

Samples were collected in the Esclangon and Faucon du Caire areas (see Fig. 1B, 2A, 2B and Table DR1 for location information) along profiles spanning elevations between 810 and 1175 m. Figure DR1 illustrates the Tertiary stratigraphic succession in the two sampled areas. In both areas, the Oligo-Miocene molasses crop out in half-windows surrounded by the Digne thrust-sheet contact, indicating that the Digne thrust-sheet previously overlay these series. A thin shallow-marine “Nummulitic” sequence is only found in the northern locality of Faucon du Caire (Dumont et al., 2012, and references therein), unconformably overlying Jurassic marls (U.1 unconformity). Sandstones in the upper part of this sequence provided samples DIG14-10A and 10B. These samples were collected in the same formation, less than 50 m apart in two beds with different grain size, to ensure the presence of suitable apatite. Following a second erosional unconformity (U.2), a much thicker, continental to littoral Oligo-Miocene sequence (Haccard et al., 1989) provided sample DIG14-9 at Faucon du Caire as well as samples DIG13-1, 3 and DIG14-4, 5, 8 (collected in the same formation, Fig. 2B) in the southern locality of Esclangon. In Esclangon, up to ~800 to 1000 m cover extends above the conglomeratic molasse, including the silty to sandy molasse and the Late-Miocene continental molasse. The latter is poorly dated around Mid to Late Miocene (Serravalian-Tortonian) and pre-dates Digne thrust-sheet emplacement (Clauzon et al., 1987; Fournier et al., 2008). Other sandstones in the half-window were also collected but did not yield apatite suitable for AFT or AHe analysis.

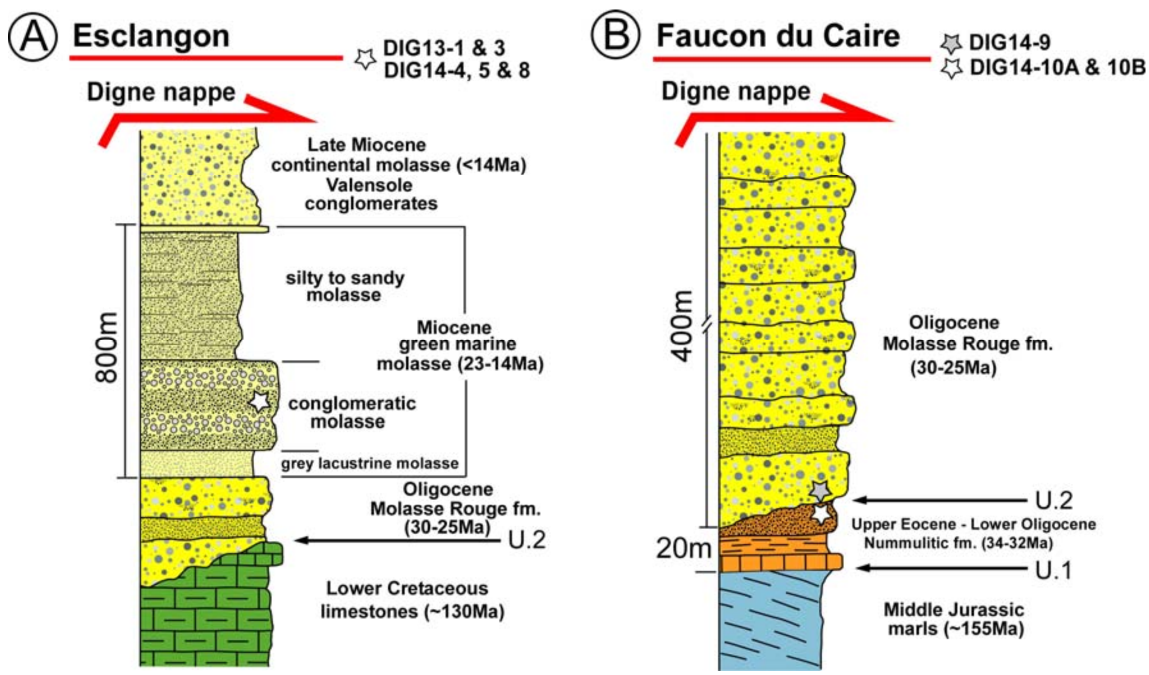


**Figure DR1:** Stratigraphic log of the Tertiary succession at the (A) Esclangon and (B) Faucon du Caire sites; stars indicate stratigraphic positions of samples.

## DR2: Analytical methods and thermal modeling

### Mineral separation

Apatite grains were separated at ISTerre (Université Grenoble-Alpes) from coarse sandstone samples using standard heavy-liquid and magnetic separation techniques.

### Apatite (U-Th-Sm)/He methods

Apatite grains were carefully selected according to their morphology and absence of visible inclusion and cracks, and placed into a platinum basket for He-extraction at Paris-Sud University (Orsay, France). Replicates were analyzed using all available apatite grains of sufficient quality per sample. The platinum baskets were heated using a diode laser allowing total He degassing; a reheat under the same conditions allowed checking for the presence of He trapped in small inclusions. The $^{4}$He content was determined by comparison with a known amount of $^{3}$He spike added during analysis. After He extraction, platinum baskets were placed into single-use polypropylene vials. Apatite grains were dissolved for 1 h at 90 °C in a 50 µl $HNO_3$ solution containing a known concentration of $^{235}$U and $^{230}$Th, and then filled with 1 ml of ultrapure MQ water. The final solution was measured for U and Th concentrations by inductively coupled quadrupole plasma mass spectrometry (ICP-QMS; series CCT Thermo-Electron) at LSCE, Gif-sur-Yvette, France. U and Th measurements followed a procedure similar to that of Evans et al. (2005). The analysis was calibrated using external age standards, including Limberg Tuff and Durango apatite, which provided mean AHe ages of 16.4 ± 1.5 Ma and 30.8 ± 1.6 Ma, respectively. These values are in agreement with literature data; that is, 16.8 ± 1.1 Ma for the Limberg Tuff (Kraml et al., 2006), 31.02 ± 0.22 Ma for Durango (McDowell et al., 2005). Single ages were corrected using the calculated ejection factor $F_T$, determined using the Monte Carlo simulation technique of Ketcham et al. (2011); the equivalent-sphere radius was calculated using the procedure of Gautheron and Tassan-Got (2010). (U-Th-Sm)/He data are reported in Table 2 and ages are shown as a function of U and Th content (expressed as eU) in Figure DR2. The 1σ error on single-grain AHe ages should be considered as 9%, reflecting the sum of errors in the ejection-factor correction and age dispersion of the standards.

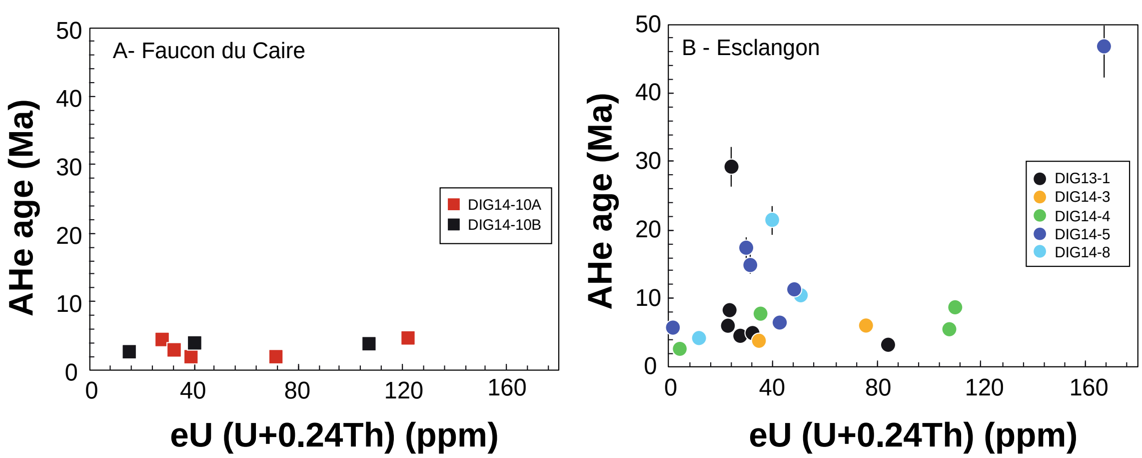


**Figure DR2:** AHe age as a function of the effective uranium (eU) content, for (A) Faucon du Caire and (B) Esclangon samples. Each dated sample is indicated by a specific color.

## AFT dating methods

For fission-track analysis, apatite grains were mounted in epoxy, polished and etched in 5M $HNO_3$ for 20 seconds at 20±1 °C. AFT ages were obtained using the external detector method following the zeta procedure (Hurford and Green, 1982) with a zeta value of 359±8 (J. Barbarand) for the CN5 dosimeter glass. Apatite mounts were covered by muscovite foils as external detectors and irradiated at the Garching facility (München, Germany) with a nominal fluence of $5\times10^{15}$ neutrons/cm$^2$. After irradiation, detectors were etched for 20 minutes in 40% HF at 20±1 °C. AFT ages are reported as central ages with ±1σ errors (Galbraith and Laslett, 1996). Dpar measurements were used to characterize the chemical kinetic properties of the apatite crystals (Burtner et al., 1994). Track counting and track-length measurements were performed using a Leica optical microscope at a magnification of 1000×. Track lengths were measured, according to the recommendations of Laslett et al. (1994), using a digitizing tablet linked to a computer. AFT data were interpreted using the BinomFit software to statistically decompose sample grain-age distributions (see Brandon, 1996 for more details). The results are presented in Table DR3; Figure DR3 shows radial plots for each sample analyzed.

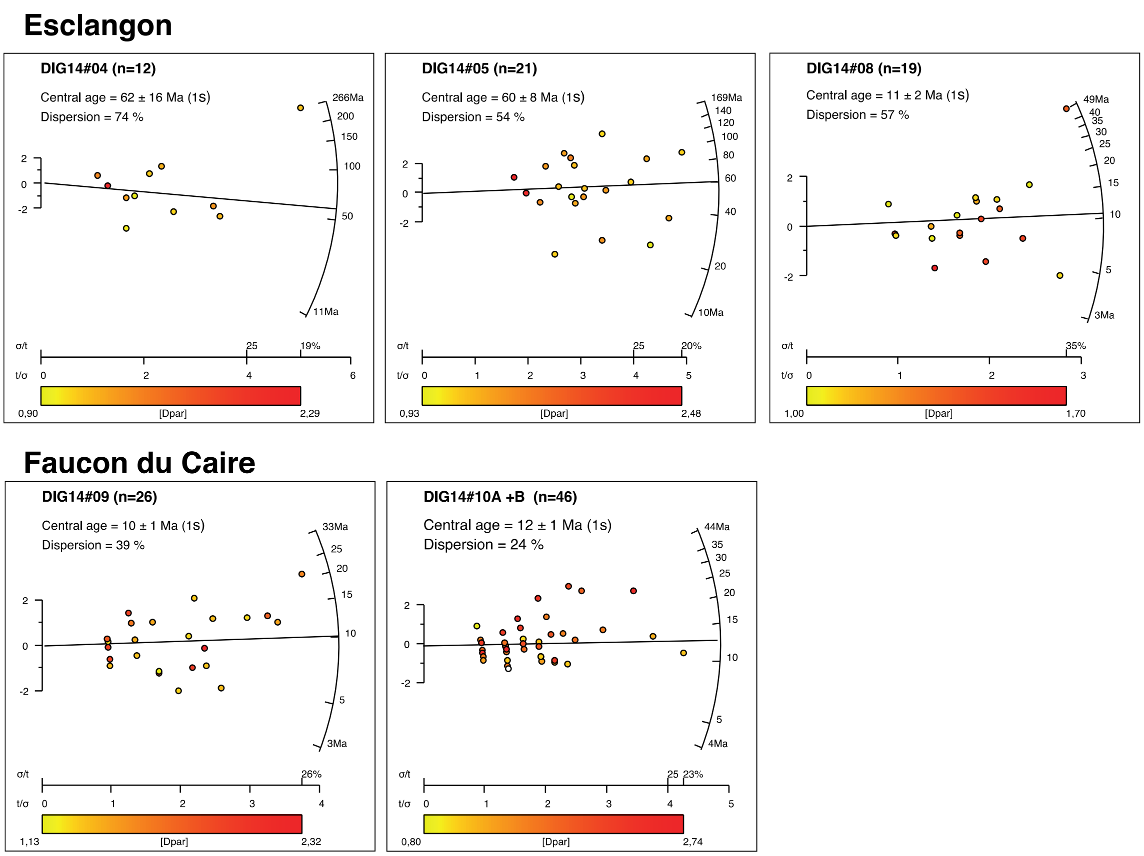


**Figure DR3:** Radial-plot representation of the AFT counting data of Esclangon and Faucon du Caire samples. Note that samples DIG14-10A and 10B have been plotted together because they are from the same formation and location.

**Thermal history modeling**

We used QTQt software (Gallagher et al., 2009; Gallagher, 2012) to extract optimal thermal histories (T-t paths) from the AHe and AFT data by a Markov-Chain Monte-Carlo (MCMC) sampling method. The inversion code incorporates recent kinetic models of He diffusion in apatite proposed by Flowers et al. (2009) and Gautheron et al. (2009), and the multi-kinetic AFT annealing model of Ketcham et al. (2007). The Bayesian transdimensional inversion approach used in this study (Gallagher, 2012) tries to balance the complexity of the inferred thermal history models with the fit to the data. This is known as natural parsimony and is implicit in the adopted method. The idea is to avoid over-interpreting the data or introducing features (structure in the thermal history) that are not required to fit the data.

For the Esclangon and Faucon du Caire areas, the parameter space (time t and temperature T, 120±120 Ma; 70±70°C) has been selected to introduce possible different pre-depositional exhumation histories for different grain populations, constituted by detrital material derived from various sources. They include Late-Eocene to Early-Oligocene fluvial and Miocene marine molasses, constituted by detrital material probably sourced from: (1) South Provençal-Corsica-Sardinia and Massif Central basement exhumed during Jurassic-Cretaceous to Paleogene times, as recorded by low-temperature thermochronology (e.g., Gautheron et al., 2009, and references therein); (2) the internal zones of the western Alps that were rapidly exhumed in the Late Eocene (e.g. Ford et al., 2006); (3) Eocene foreland-basin sandstones; and (4) Early-Oligocene volcanics (Jourdan et al., 2012, Schwartz et al., 2012). Consequently, pre-depositional AFT and AHe ages are expected to range from Triassic to Oligocene.

Two additional geological constraints have been imposed: (1) depositional ages of 20±2 Ma for Esclangon and 30±8 Ma for Faucon du Caire, during which time the samples were at surface temperature (10±10°C); (2) overthrusting of the Esclangon and Faucon du Caire areas by the Digne thrust sheet should be younger than the oldest reset AFT age (including its uncertainty), which is ~14 Ma for Faucon du Caire and ~13 Ma for Esclangon. In detail, nearby Esclangon, the youngest dated sediments overlain by the Digne Nappe are Serravallian-Tortonian in age (Clauzon et al., 1987). Thermal history simulations are the product of 40,000 iterations, which is a sufficient number to obtain a stable and robust solution (see discussion in Gallagher, 2012). Chemical composition ranges of the analyzed apatites have been taken into consideration for both AFT and AHe modeling, by imposing the mean measured Dpar values for the sample, following Gautheron et al. (2013).

Thermal history simulation results for Faucon du Caire and Esclangon are reported in Figs. 2E and 2F. The thermal histories results are strongly impacted by the reset AFT data for the lower-elevation samples in Esclangon and the reset data at Faucon du Caire that impose a maximum temperature of ~110±5 °C at ~10 Ma (see Table DR3). Additionally, the youngest AHe ages from both locations impose onset of cooling at ~6 Ma; this is especially well constrained for the Esclangon area (Figs. 2E, 2F). It is important to note that, while the true thermal history may be more complex than that inferred by the inverse modeling (Gallagher, 2012), the data do not contain enough information to justify this more complex thermal history over the simpler one.

## Section DR3: Estimates of the emplacement time and thickness of the Digne thrust-sheet

### Digne thrust-sheet emplacement time

The emplacement time of the Digne thrust-sheet is not well defined in the Faucon du Caire area; our thermochronological data and inversion results provide important new constraints on this timing. As shown in Fig. 2E, the temperature-time path of the Eocene and Oligocene sediments shows that they reached maximum temperatures around ~12 Ma. Because of the rapid thermal equilibration during burial under a few-km thick thrust sheet (<0.1 Ma; Husson and Moretti, 2002), we propose that this timing records the emplacement of the Digne thrust sheet in the Faucon du Caire area. In the Esclangon area, as illustrated in the sedimentary log (Fig. DR1), the sampled Early-Miocene sandstones have been buried ~800 to 1000 m below Early- to Late-Miocene sediments. This burial is, however, not sufficient to affect the AHe and AFT systems, because the samples would only have been heated to 35 - 40°C, for a surface temperature of 10 °C and a geothermal gradient of 25 to 30 °C/km. The partial to total resetting of both thermochronometers shown by the studied samples is therefore the result of underthrusting below the Digne thrust-sheet. The thermal modeling refines the timing of maximum burial to ~9 Ma (Fig. 2F), demonstrating that the Digne thrust-sheet was emplaced above our samples at this time. Our data imply that the (poorly dated) Valensole series immediately in front of the Digne thrust-sheet were deposited during the Serravalian-early Tortonian (i.e., before ~9 Ma).

### Digne thrust-sheet thickness estimation

From the determined thermal history (Figs. 2E and 2F), for a mean surface temperature of 10 °C and a geothermal gradient ranging from 25 to 30 °C/km, our data show that the samples were buried to depths of 3.3 to 4.0 km at both sites.

At Faucon du Caire, the samples may have been partially reset by sedimentary burial before emplacement of the Digne thrust-sheet, but were subsequently completely reset for both thermochronometers. The inferred thermal history (Fig. 2E) demonstrates burial to 110±5 °C, implying that the Digne thrust-sheet was up to 3.3 to 4.0 km thick at Faucon du Caire. For Esclangon, the thermal history (Fig. 2F) reveals that the samples were buried at maximum to 110±5 °C, similar to Faucon du Caire. However, at Esclangon, Miocene sediments are present in the syncline stratigraphically above our samples (see Fig. 2B). One can estimate that the samples were buried by ~1 km of Miocene sediments, indicating a 2.3 to 3 km thick Digne thrust-sheet at this site. These estimates for lateral along-strike variations in the thickness of the Digne thrust sheet is similar to that proposed by Ford et al. (1999).

**Table DR1:** Sample descriptions and locations

| Sample name | Age / rock type | Latitude (N) | Longitude (E) | Elevation (m) |
|---|---|---|---|---|
| | **Esclangon** | | | |
| **DIG13-1** | Miocene green marine molasse | 44°12’30" | 6°16’44" | 1114 |
| **DIG13-3** | Miocene green marine molasse | 44°12'36" | 6°16'22" | 810 |
| **DIG14-4** | Miocene green marine molasse | 44°12’53" | 6°15’53" | 1175 |
| **DIG14-5** | Miocene green marine molasse | 44°12’53" | 6°15’59" | 1138 |
| **DIG14-8** | Miocene green marine molasse | 44°12'40" | 6°16'24" | 812 |
| | **Faucon du Caire** | | | |
| **DIG14-9** | Oligocene Molasse Rouge fm. | 44°23'6.03" | 6° 4'40.34" | 875 |
| **DIG14-10A** | Upper Eocene Nummulitic fm. | 44°23'37.84" | 6° 5'36.05" | 960 |
| **DIG14-10B** | Upper Eocene Nummulitic fm. | 44°23'38.30" | 6° 5'39.40" | 1005 |

**Table DR2:** Apatite (U-Th-Sm)/He data

| Sample | Weight (µg) | $F_T$ | Rs [$] (µm) | $^4He$ (nmol/g) | U (ppm) | Th (ppm) | Sm (ppm) | eU (ppm) | Th/U | Age (Ma) | Age c * (Ma) |
|---|---|---|---|---|---|---|---|---|---|---|---|
| | | | | | | **Esclangon** | | | | | |
| **DIG13-1A** | 3.5 | 0.74 | 52 | 0.67 | 23 | 37 | 117 | 32.3 | 1.6 | 3.9 | 5.0±0.5 |
| **DIG13-1B** | 4.0 | 0.76 | 59 | 1.11 | 35 | 202 | 254 | 83.9 | 5.7 | 2.5 | 3.1±0.3 |
| **DIG13-1bisA** | 3.4 | 0.78 | 52 | 0.54 | 14 | 38 | 471 | 22.9 | 2.7 | 4.3 | 6.1±0.5 |
| **DIG13-1bisD** | 6.2 | 0.77 | 53 | 2.99 | 18 | 24 | 150 | 24.1 | 1.3 | 23.0 | 29.3±2.6 |
| **DIG13-1bisC** | 7.1 | 0.79 | 54 | 0.82 | 20 | 11 | 193 | 23.2 | 0.6 | 6.5 | 8.4±0.8 |
| **DIG13-1bisB** | 7.6 | 0.79 | 55 | 0.54 | 27 | 7 | 165 | 28.4 | 0.3 | 3.5 | 4.6±0.4 |
| **DIG13-3DD** | 8.7 | 0.81 | 72 | 2.05 | 59 | 71 | 57 | 75.6 | 1.2 | 5.1 | 6.1±0.5 |
| **DIG13-3FF** | 8.5 | 0.80 | 71 | 0.63 | 32 | 12 | 196 | 34.7 | 0.4 | 3.3 | 3.9±0.4 |
| **DIG14-4A** | 5.4 | 0.83 | 82 | 0.07 | 3 | 5 | 258 | 4 | 1.8 | 3.1 | 3.8±0.2 |
| **DIG14-4B** | 1.6 | 0.74 | 54 | 2.43 | 98 | 41 | 487 | 108 | 0.4 | 4.0 | 5.4±0.5 |
| **DIG14-4D** | 2.6 | 0.72 | 48 | 1.15 | 33 | 12 | 354 | 35 | 0.4 | 5.6 | 7.8±0.7 |
| **DIG14-4F** | 2.0 | 0.74 | 54 | 3.83 | 77 | 137 | 217 | 110 | 1.8 | 6.4 | 8.6±0.8 |
| **DIG14-5A** | 3.2 | 0.81 | 76 | 2.21 | 17 | 61 | 296 | 31 | 3.7 | 12.2 | 15.0±1.3 |
| **DIG14-5B** | 4.2 | 0.80 | 71 | 34.19 | 103 | 265 | 383 | 167 | 2.6 | 37.4 | 46.9±4.2 |
| **DIG14-5C** | 5.2 | 0.82 | 78 | 0.11 | 1 | 4 | 275 | 2 | 4.8 | 8.9 | 10.9±1.0 |
| **DIG14-5E** | 6.6 | 0.84 | 91 | 2.57 | 47 | 7 | 218 | 48 | 0.1 | 9.5 | 11.3±1.0 |
| **DIG14-5F** | 7.5 | 0.82 | 81 | 1.29 | 39 | 13 | 238 | 42 | 0.3 | 5.4 | 6.5±0.6 |
| **DIG14-5G** | 5.0 | 0.81 | 77 | 2.40 | 29 | 3 | 223 | 30 | 0.1 | 14.1 | 17.3±1.6 |
| **DIG14-8A** | 1.3 | 0.67 | 42 | 5.35 | 18 | 12 | 476 | 21 | 0.7 | 40.6 | 60.4±5.4 |
| **DIG14-8B** | 3.4 | 0.74 | 53 | 0.20 | 6 | 23 | 71 | 11 | 3.8 | 3.1 | 4.1±0.4 |
| **DIG14-8C** | 1.5 | 0.69 | 44 | 3.22 | 32 | 32 | 106 | 40 | 1.0 | 14.7 | 21.5±1.9 |
| **DIG14-8D** | 5.1 | 0.77 | 61 | 2.29 | 49 | 4 | 214 | 50 | 0.1 | 8.2 | 10.6±1.0 |
| | | | | | | **Faucon du Caire** | | | | | |
| **DIG14-10B-A** | 3.0 | 0.79 | 67 | 1.80 | 68 | 164 | 263 | 107 | 2.4 | 3.1 | 3.9±0.4 |
| **DIG14-10B-B** | 5.7 | 0.84 | 87 | 0.20 | 5 | 43 | 164 | 15 | 9.0 | 2.5 | 2.9±0.2 |
| **DIG14-10B-C** | 3.0 | 0.79 | 68 | 0.71 | 26 | 59 | 358 | 40 | 2.3 | 3.1 | 3.9±0.3 |
| **DIG14-10A-A** | 6.4 | 0.82 | 81 | 0.40 | 9 | 125 | 218 | 39 | 13.7 | 1.8 | 2.2±0.2 |
| **DIG14-10A-1** | 10.9 | 0.82 | 77 | 0.46 | 13 | 82 | 160 | 33 | 6.3 | 2.5 | 3.1±0.3 |
| **DIG14-10A-3** | 5.7 | 0.83 | 82 | 0.60 | 32 | 164 | 229 | 71 | 5.1 | 1.6 | 1.9±0.2 |
| **DIG14-10A-4** | 3.2 | 0.74 | 54 | 2.33 | 72 | 209 | 314 | 122 | 2.9 | 3.5 | 4.7±0.4 |
| **DIG14-10A-6** | 5.3 | 0.81 | 76 | 0.60 | 11 | 70 | 362 | 28 | 6.5 | 3.7 | 4.5±0.4 |

[$] $R_s$ is the sphere equivalent radius calculated using the code of Gautheron and Tassan-Got (2010).

* AHe age corrected for the ejection factor (Ketcham et al., 2011).

**Table DR3:** Apatite fission-track data

| | n | $\rho s \times 10^5$ (tracks/cm$^2$) (Ns) | $\rho i \times 10^5$ (tracks/cm$^2$) (Ni) | $\rho d \times 10^5$ (tracks/cm$^2$) (Nd) | U (ppm) | P($\chi$2) | D (%) | Central age (Ma) | Dpar (µm) |
|---|---|---|---|---|---|---|---|---|---|
| | | | | **Esclangon** | | | | | |
| **DIG14-4** | 12 | 0.555<br>(183) | 0.630<br>(208) | 5.307<br>(5612) | 15 | 0 | 74 | 62±16 | 1.3±0.4 |
| **DIG14-5** | 21 | 0.447<br>(381) | 0.812<br>(692) | 5.363<br>(5612) | 18 | 0 | 54 | 60±8 | 1.4±0.4 |
| **DIG14-8** | 19 | 0.103<br>(77) | 1.109<br>(832) | 5.474<br>(5612) | 25 | 0 | 60 | 11±2 | 1.3±0.2 |
| | | | | **Faucon du Caire** | | | | | |
| **DIG14-9** | 26 | 0.107<br>(120) | 1.158<br>(1294) | 5.529<br>(5612) | 26 | 1.7 | 39 | 10±1 | 1.6±0.3 |
| **DIG14-10A** | 21 | 0.106<br>(112) | 0.868<br>(916) | 5.58<br>(5612) | 19 | 8.8 | 13 | 12±1 | 1.8±0.5 |
| **DIG14-10B** | 25 | 0.056<br>(71) | 0.480<br>(604) | 5.640<br>(5612) | 10 | 29.7 | 29 | 12±2 | 1.9±0.5 |

Notations: n: number of apatite crystals counted; ρ: track density ($\times 10^5$ tracks/cm²); subscripts s, i and d denote spontaneous, induced and dosimeter, respectively; U: mean uranium content; P($\chi$2): probability of obtaining Chi-square value ($\chi$2) for n degrees of freedom (where n = number of crystals - 1); D: age dispersion (Galbraith and Laslett, 1996); Dpar: mean maximum diameter of fission-track etch figures parallel to the c-axis. Central ages have been reported for each sample with a confidence interval of $\pm 1\sigma$ and are calculated using the zeta-calibration method (Hurford, 1990) with $\zeta = 359 \pm 8$ (J.B.) on CN-5 glass.

## REFERENCES CITED

Brandon, M.T., 1996, Probability density plot for fission track grain-age samples. Radiation Measurements v. 26, pp 663-676.

Burtner, R.L., Nigrini, A., Donelick, R.A., 1994, Thermochronology of lower cretaceous source rocks in the Idaho-Wyoming thrust belt. Am. Ass. Petrol. Geol. Bull. V. 78, p. 1613-1636.

Clauzon G., Aguilar J.P., Michaux J., 1987, Mise en évidence d'un diachronisme de 5 Ma au mur de la molasse miocène de Valensole (Alpes de Haute Provence, France). Révisions chronostratigraphiques et implications géodynamiques. C. R. Acad. Sc. Paris, v. 305, p. 133-137.

Dumont T., Schwartz S., Guillot S., Simon-Labric T., Tricart P., Jourdan S., 2012. Structural and sedimentary record of the Oligocene revolution in the Western Alpine arc. Jour. Geodyn., 56-57, p. 18-38.

Evans, N.J., Byrne, J.P., Keegan, J.T., Dotter, L.E., 2005, Determination of uranium and thorium in zircon, apatite, and fluorite: Application to laser (U–Th)/He thermochronology. Journal of analytical Chemistry, v. 60, p. 1300–1307.

Flowers, R., Ketcham, R.A., Shuster, D., Farley, K.A., 2009. Apatite (U–Th)/He thermochronology using a radiation damage accumulation and annealing model. Geochimica et Cosmochimica Acta, v. 73, p. 2347–2365.

Fournier, M., Agard, P., Petit, C., 2008, Micro-tectonic constraints on the evolution of the Barles half-window (Digne nappe, southern Alps). Implications for the timing of folding in the Valensole foreland basin: Bulletin de la Société Géologique de France, v.179, p. 551–568.

Ford, M., Lickorish, W.H. and Kusznir, N.J., 1999. Tertiary foreland sedimentation in the Southern Subalpine Chains, SE France: a geodynamic appraisal. Basin Research, v.11, p. 315-336, doi:10.1046/j.1365-2117.1999.00103.x.

Ford, M., Duchêne, S., Gasquet, D., and Vanderhaeghe, O., 2006, Two-phase orogenic convergence in the external and internal SW Alps: Journal of the Geological Society, v. 163, p. 815–826, doi:10.1144/0016-76492005-034.

Galbraith, R.F., Laslett, G.M., 1996. Statistical modelling of thermal annealing of fission tracks in apatite. Geochim. Cosmochim. Acta, v. 60, p. 5117-5131.

Gallagher, K., Charvin, K., Nielsen, S., Sambridge, M., Stephenson, J., 2009, Markov chain Monte Carlo (MCMC) sampling methods to determine optimal models, model resolution and model choice for Earth Science problems. Marine and Petroleum Geology, v. 26, p. 525–535.

Gallagher, K., 2012. Transdimensional inverse thermal history modeling for quantitative thermochronology. Journal of Geophysical Research, v. 117, b02408.

Gautheron, C., Tassan-got, L., Barbarand, J., Pagel, M., 2009. Effect of alpha-damage annealing on apatite (U–Th)/He thermochronology. Chemical Geology, v. 266, p. 166–179.

Gautheron, C., Tassan-Got, L. 2010. A Monte Carlo approach of diffusion applied to noble gas/helium thermochronology. Chemical Geology, v. 273, p. 212–224.

Gautheron, C., Barbarand J., Ketcham R., Tassan-Got L., van der Beek P. A., Pagel M., Pinna-Jamme R., Couffignal F., Fialin M., 2013. Chemical influence on a-recoil damage annealing in apatite: implications for (U–Th)/He dating. Chemical Geology. v. 351, p. 257–267.

Haccard, D., Beaudouin B., Gigot P., Jorda M. 1989. Notice explicative de la carte géologique de France (1/50000), feuille La Javie (918). Bur. Rech. Géol. Min., Orléans, 152 p.

Hurford, A.J., Green, P.F., 1982. A users' guide to fission track dating calibration. Earth Planet. Sci. Lett., v. 59, p. 343-354.

Hurford, A.J., 1990. Standardization of fission track dating calibration : Recommendation by the Fission Track Working Group of the I.U.G.S. subcommission on Geochronology. Chem. Geol. v. 80, p. 171-178.

Husson, L., and Moretti, I., 2002. Thermal regime of fold and thrust belts—an application to the Bolivian sub Andean zone. Tectonophysics, 345: 253-280.

Jourdan, S., Bernet, M., Schwartz, S., Guillot, S., Tricart, P., Chauvel, C., Dumont, T., Montagnac, G., and Bureau, S., 2012, Tracing Oligocene-Miocene evolution of the western Alps topography with geochemical analyses and Raman spectroscopy of foreland basin deposits: The Journal of Geology, v. 120, p. 603–624, doi:10.1086/667813.

Ketcham, R.A., Carter, A., Donelick, R.A., Barbarand, J., Hurford, A.J., 2007, Improved modeling of fission-track annealing in apatite: American Mineralogist, v. 92, p. 799–810.

Ketcham, R.A., Gautheron, C., Tassan-Got, L., 2011. Accounting for long alpha-particle stopping distances in (U–Th–Sm)/He geochronology: Refinement of the baseline case. Geochimica et Cosmochimica acta, v. 75, p. 7779–7791.

Kraml, M., Pik, R., Rahn, M., Selbekk, R., Carignan, J., Keller, J., 2006. A new multi-mineral age reference material for $^{40}Ar/^{39}Ar$, (U–Th)/He and fission track dating methods: The Limberg t3 tuff. Geostandards and Geoanalytical Research, v. 30, p. 73–86.

Laslett, G.M., Gleadow, A., Duddy, I.R., 1994. The relationship between fission-track length and track density in apatite. Nuclear Tracks, v. 9, p. 29-38.

McDowell, F.W., McIntosh, W.C., Farley, K.A., 2005. A precise $^{40}Ar$–$^{39}Ar$ reference age for the Durango apatite (U–Th)/He and fission-track dating standard. Chemical Geology, v. 214, p. 249–263.

Schwartz, S., Guillot, S., Tricart, P., Bernet, M., Jourdan, S., Dumont, T. and Montagnac, G., 2012, Source tracing of detrital serpentinite in the Oligocene molasse deposits from western Alps (Barrême basin): implications for relief formation in the internal zone. Geological Magazine, v. 149, p. 846–851, doi: 10.1017/S0016756811001105.